Supporting Information

to

Metalloregulator CueR biases RNA polymerase's kinetic sampling of dead-end or open complex to repress or activate transcription

Danya J. Martell[a], Chandra P. Joshi[a,1], Ahmed Gaballa[b], Ace George Santiago[a], Tai-Yen Chen[a], Won Jung[a], John D. Helmann[b], Peng Chen[a,*]

[a] Departments of Chemistry and Chemical Biology, and [b] Microbiology, Cornell University, Ithaca, NY 14853

[1] Present address: Department of Cell Biology, Duke University Medical Center, Durham, NC 27710

* Correspondence: pc252@cornell.edu

Table of content

1. Materials, methods, and experimental strategy

a. DNA design, fluorescent probe location, and preparation

Two different DNA labeling schemes were used to examine RNAP–P*copA* interactions (Fig. S1). In both schemes, the DNA strands contain the complete promoter region of the *copA* gene regulated by CueR, including the dyad symmetric sequence recognized by CueR, the −35 and −10 RNAP recognition elements, as well as the entire DNA footprint region of CueR determined by Outten et al (1). Both DNAs also include the entire expected RNAP footprint region, determined by aligning the RNAP footprint at the promoter region of *merTPAD* operon that MerR regulates (2).

In one scheme, the DNA, referred to as P$copA_{Cy3@-41}$, is 120 base-pairs long and spans from position −59 to +61 around the promoter. It is labeled with Cy3 at an amine modified T at position −41 of the nontemplate strand through NHS ester labeling (Lumiprobe, cat# 11320) (Fig. S1A). Biotin-TEG is attached to the 5′ end of the template strand; this labeling scheme ensures that only double-strand DNA was immobilized and fluorescently imaged in the experiments. The DNA was made via PCR using Cy3 and biotin-TEG labeled primers with AccuprimerPfx DNA Polymerase (Life Technologies, cat# 12344024). The primers, 5′-CCCGCCTGGTTTATTAAT/iAmMC6T/TCTTGACC-3′ (which was labeled by Cy3 first) and 5′-/5BioTEG/TCCAGGGTCAGGTCGATAGTTTGTGAC-3′, were purchased from Integrated DNA Technologies (IDT; Coralville, IA). The PCR product was purified using Wizard SV Gel and PCR Clean-Up System (Promega, cat# A9281). All DNAs were confirmed by gel electrophoresis, and stored in nuclease free water.

In the other scheme, the DNA, referred to as P$copA_{Cy3@-5}$, is 100 base-pairs long and spans from position −59 to +41 around the promoter. It is labeled with Cy3 at an amine modified T at position −5 of the template strand through NHS ester linkage. Biotin-TEG is attached to the 3′ end of the nontemplate strand (Fig. S1B). Both strands of P$copA_{Cy3@-5}$ were purchased from IDT, labeled with Cy3 (for the template strand), and annealed together.

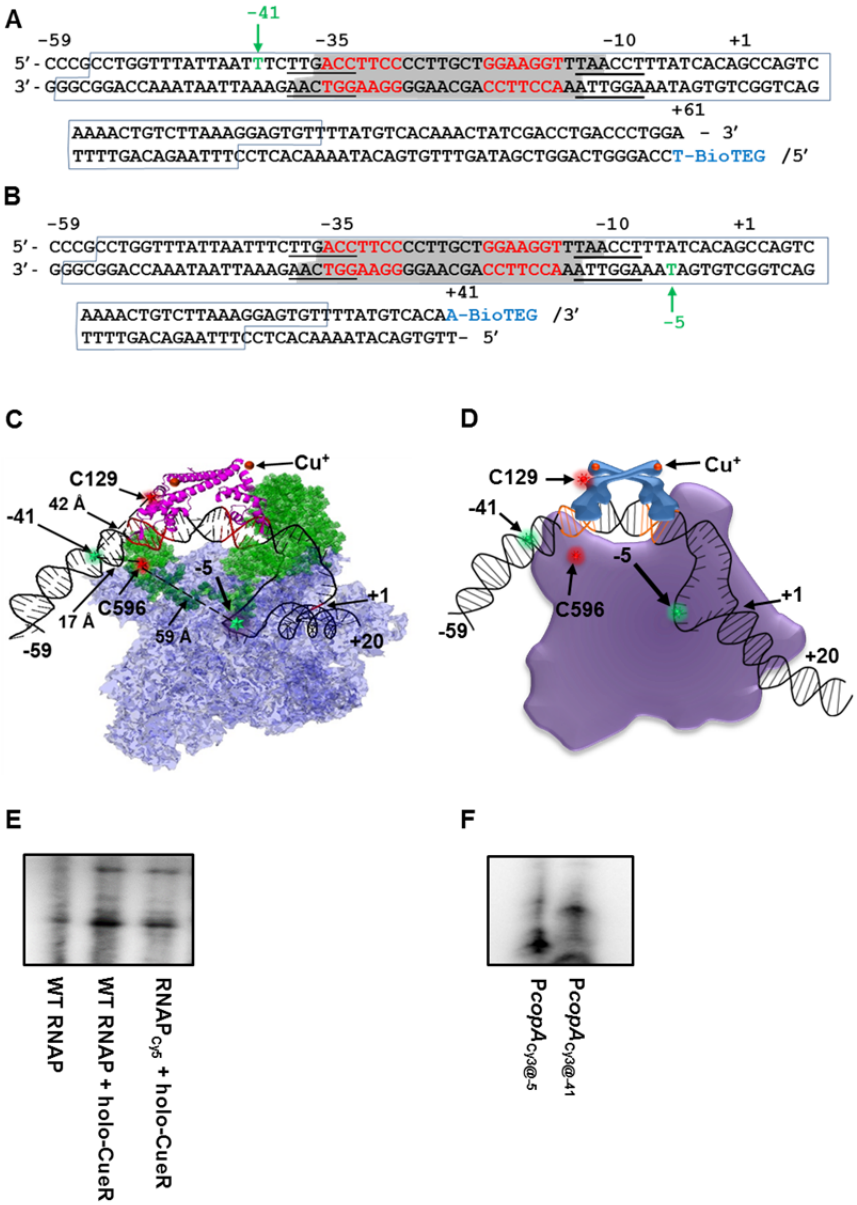

Fig. S1. DNA sequences and structure model of RNAP-DNA-CueR complex. (A) Sequence of the P*copA*$_{Cy3@-41}$ DNA derived from *E. coli copA* gene promoter region. The −35 and −10 elements are underlined. The RNAP footprint at a MerR-regulated promoter is overlaid here (2), shown by the boxed region. The dyad symmetric sequence that CueR recognizes is shown in red. The CueR footprint (1) is shaded grey. The Cy5 dye is attached at the −41 position (green vertical arrow) via an amine modified T (denoted in green). The Biotin-TEG is attached to the 5'-end of the +61 position (shown in blue) for immobilizing the DNA. (B) Same as A but for the P*copA*$_{Cy3@-5}$ DNA. (C) A structural model of a RNAP–DNA–CueR complex, where CueR is shown in magenta, RNAP core enzyme is shown in purple, and σ^{70} factor is shown in green. The position of the −41 or −5 Cy3 label is indicated by an arrow and shown as a green sphere on the DNA strand. The transcription start site (+1) is also noted on the DNA. The position of the Cy5 label on CueR is indicated by an arrow (labeled C129) and shown as a red sphere on CueR. The orange color on the DNA marks the positions of the dyad symmetric sequence recognized by CueR. The position of the Cy5 label on RNAP is indicated by an arrow (labeled C596) and shown as a red sphere on σ^{70}. The Cy3–Cy5 anchor-to-anchor distances for RNAP-P*copA* or CueR-P*copA* smFRET are denoted. (D) A cartoon representation of the structural model in C. For simplification, σ^{70} is not separately drawn out in the cartoon representation of holo RNAP. (E) Gel image of RNA production from the *in vitro* transcription run-off assay with the 315-bp DNA fragment in the presence of wild type RNAP only, or in

the presence of wild type RNAP and 200 nM holo-CueR, or in the presence of $RNAP_{Cy5}$ and 200 nM holo-CueR, demonstrating $RNAP_{Cy5}$ is functional. (F) Gel image of RNA production from the *in vitro* transcription run-off assay using P*copA*$_{Cy3@-41}$ (100 bp) or P*copA*$_{Cy3@-5}$ (120 bp) as templates in the presence of wild type RNAP and 200 nM holo-CueR, demonstrating that both these two labeled DNA can act as transcription templates. Due to the smaller transcript lengths here than those in E, the gel here was run for a shorter time, resulting less separated bands.

b. Structural model of RNAP-DNA-CueR complex for selecting locations for fluorescent probes

The locations of the donor, Cy3, and acceptor, Cy5, fluorescent probes are shown on a structural model of an RNAP–DNA–CueR complex in Fig. S1C. The model was generated by overlaying the DNA-bound *E. coli* RNAP holoenzyme structure (pdb 3IYD) (3) and the holo-CueR structure (pdb 1Q05) (4) on top of the structure of the MtaN–DNA complex (pdb 1R8D) (5, 6). MtaN is a homologue of CueR; it responds to organic drugs instead of metal ions. The original RNAP-DNA structure consists of the RNAP holoenzyme, the catabolite activator protein (CAP), a CAP-dependent promoter DNA fragment containing positions −78 to +20, and a premelted transcription bubble (3). CAP was removed from our model and so was the DNA upstream of position −59. The structure of MtaN–DNA complex was used to determine the approximate location of CueR in the RNAP-DNA complex. The cartoon representation in Fig. S1D is the basis of the cartoons used throughout the text to depict the RNAP–DNA–CueR complexes.

For the RNAP construct, $RNAP_{R596C}$, the Cy5 was incorporated at the residue R596C of σ^{70} located in region 4, as previously described (7-10). Based on the structural model (Fig. S1C), the Cy3–Cy5 anchor-to-anchor distance in the $RNAP_{Cy5}$–P*copA*$_{Cy3@-41}$ is about 17 Å, and the Cy5 on P*copA*$_{Cy5@-41}$ is pointed away from RNAP and thus should not affect RNAP binding. It is also close to the −40 position, which was labeled by Mukhopadhyay and Kapanidis *et al.* in studying RNAP interactions with optimal promoters and was shown to be non-disruptive (11, 12).

Based on the same model, the Cy3–Cy5 anchor-to-anchor distance in the $RNAP_{Cy5}$–P*copA*$_{Cy3@-5}$ complex is about 59 Å, and the Cy5 at −5 position on P*copA* should also not affect RNAP binding based on the structural model. Moreover, this −5 position is close to the −3 position, which was previously labeled by Robb *et al.* and shown to be functionally non-disruptive for RNAP interactions with optimal promoters (13). As the −5 location is within the transcription bubble region, its FRET with Cy5 on RNAP should thus be sensitive to open complex formation. Bubble formation in the open complex is expected to pull the two DNA strands toward opposite directions, and based on the structural model in Fig. S1C, in the transcription bubble, the strand containing Cy3 is closer to the Cy5 on RNAP than the other strand, suggesting that bubble formation would bring Cy3 closer to the Cy5. Both the −41 and −5 position are outside the region where CueR binds, and thus should not affect CueR binding.

For $CueR_{Cy5}$, Cy5 is attached to the surface-exposed C129 of one monomer of the dimeric CueR, as we previously reported (14); this labeling position is located near the C-terminal within the metal-binding domain of CueR (Fig. S1C). This labeling scheme makes a singly-labeled CueR homodimer asymmetric, giving rise to two different binding orientations on DNA. Based on the structural model (Fig. S1C), the Cy3–Cy5 anchor-to-anchor distances in a $CueR_{Cy5}$–P*copA*$_{Cy3@-41}$ complex are about 69 Å and 42 Å for the two binding orientations. One of the two binding orientations could be readily resolved in the E_{FRET} histogram at $E_{FRET} \sim 0.81$ (Fig. 5A), corresponding to the shorter-distanced orientation; the orientation with longer anchor-to-anchor distance is buried by the free DNA state in the E_{FRET} histogram (Fig. 5A), but can be seen in the E_{FRET} vs. time trajectories ($E_{FRET} \sim 0.18$; Fig. S12A).

c. σ^{70} mutant, expression, purification, and fluorescence labeling

The pGEMD(-Cys) derivative plasmid, containing the σ^{70} mutant with a single Cys residue at position 596 (i.e., R596C), was provided by R. Ebright (Rutgers University). It was expressed, purified, and labeled as previously described (11). The transcriptional activity of holo RNAP containing this labeled σ^{70} mutant was confirmed by Ebright and coworkers to be indistinguishable from unlabeled *E. coli* RNAP (11). Briefly, the pGEMD(-Cys) vector was transformed into and expressed in BL21(DE3). Cells were harvested by centrifugation and lysed by sonication. Cell lysate was centrifuged and precipitate was washed with lysis buffer containing 0.2 mg/ml lysozyme and 0.5% Triton X-100 and then 0.5% Triton X-100 and 1 mM DTT lysis buffer. The washed precipitate was solubilized in a buffer containing 6 M guanidine-HCL, 50 mM Tris-HCl (pH 7.9), 10 mM $MgCl_2$, 10 μM $ZnCl_2$, 1 mM EDTA, 10 mM DTT, and 10% glycerol and then dialyzed against a buffer containing 20 mM Tris-HCl (pH 7.9), 0.1 mM EDTA, 0.1 mM DTT, and 5% glycerol at 4°C for 20 hours. The sample was then purified through Mono Q anion exchange column and fractions containing the σ^{70} mutant were identified by SDS-PAGE. The purified σ^{70} mutant was then labeled with Cy5-maleimide (Invitrogen) at the targeted cysteine. The Cy5 was added to purified σ^{70} ([dye]:[σ^{70}] = 3:1) in 100 mM phosphate buffer solution at pH 7. The reaction mixture was kept on shaker at 4°C for ~16 hours. Labeled σ^{70} was then purified by a gel filtration column (HILOAD 26/60 Superdex 200 PR, GE Healthcare), and by an anion exchange column (Mono Q 5/50 GL, GE Healthcare). The dye:protein ratio of the labeled σ^{70} was determined to be ~0.9. The extinction coefficient of 250,000 $M^{-1}cm^{-1}$ at 650 nm was used for determining the Cy5 concentration. Similarly, the calculated extinction coefficient of 41,370 $M^{-1}cm^{-1}$ at 280 nm (determined from the sequence using Lasergene, DNASTAR) was used for determining the σ^{70} concentration. The labeled σ^{70} was stored at −80°C in 20 mM Tris-HCl (pH 7.9), 100 mM NaCl, 0.1 mM EDTA, 0.1 mM DTT, and 50% glycerol.

To form the labeled holo RNAP (i.e., $RNAP_{Cy5}$), wild type (WT) *E. coli* RNA polymerase core enzyme (Epicenter) was mixed with a 3× molar excess of $\sigma^{70}{}_{Cy5@R596C}$ and incubated at 25°C for 20 minutes. The unlabeled holo RNAP was purchased commercially (Epicenter, cat# S90050).

d. CueR expression, purification, fluorescence labeling, and copper removal

The CueR variant, $CueR_{C129}$, was created, expressed and purified to be labeled with a single FRET acceptor, Cy5, at the specific cysteine at position 129, as we reported previously (14). The variant is functionally active as we previously showed (14). Briefly, $CueR_{C129}$ was cloned in a pET30a vector and expressed in BL21(DE3) strain. The cell lysate was purified by precipitation and then HiPrep gel filtration. The collected fractions were further purified through a Heparin affinity column followed by a Superdex gel filtration column, and lastly an anion exchange Mono Q column. CueR was metallated by adding $CuSO_4$ solution in the presence of excess TCEP. The Cu^+ binding protects the metal-binding cysteines of CueR from dye labeling. The protein was then labeled. CueR is encoded as a monomer but it is purified as a stable homodimer, thus the labeling reaction generates a mixture of unlabeled, mono-labeled and bi-labeled species. The labeled protein was purified using an anion exchange column (Mono Q 5/50 GL) to obtain the mono-labeled fraction. The dye:protein ratio of the resulting holo-CueR protein of ~0.8. The labeled holo-CueR could be converted to the apo form by removing the bound copper using KCN (at 1000× excess) (4). Extracted copper and excess KCN were then removed by a desalting column (HiTrap, GE Healthcare). The dye:protein ratio of the resulting apo-protein was ~0.9. The copper content of the apo-protein was confirmed to be <4% via BCA copper quantification assay (15). The labeled holo and apo proteins were stored at −80°C in 50 mM pH 7.0 Tris Buffer with ~250 mM NaCl and 30% glycerol.

e. In vitro transcription run-off assay demonstrates that $RNAP_{Cy5}$ is functional and both $PcopA_{Cy3@-5}$ and $PcopA_{Cy3@-41}$ are functional transcription templates.

An *in vitro* transcription run-off assay was performed by following previously reported procedures (2, 4, 16) in order to confirm that the labeled RNAP variant, $RNAP_{Cy5}$, is transcriptionally active. Using the primers 5′-TCTTTACGGACTTTTACCCGCCTGG-3′ and 5′-CCTTTGGGTGGCTTACAGATGCGTC-3′ with PCR, a 315-bp DNA fragment was copied out of the *E. coli* genome that spans the promoter and part of the *E. coli copA* gene. This fragment was used as the template for *in vitro* transcription. $RNAP_{Cy5}$ is prepared by mixing wild type (WT) *E. coli* RNAP core enzyme (Epicenter) with a 3× molar excess of $\sigma^{70}_{Cy5@R596C}$ and incubating the mixture at 25°C for 20 minutes. Transcription reactions were performed by incubating either 50 nM of *E. coli* RNAP holoenzyme (Epicenter) or 50 nM of *E. coli* $RNAP_{Cy5}$ with 20 μg/mL of the 315-bp DNA template, and 200 nM of apo $CueR_{C129}$ in a buffer solution (100 mM potassium glutamate, 10 mM pH 8 Tris-base, 1 mM $MgCl_2$, 0.1 mM EDTA, 100 μg/mL of acetylated-BSA, 1 mM $CaCl_2$, 5% glycerol, 2 mM dithiothreitol, 10 μM BCA) and 1 μM $[Cu(CH_3CN)_4]PF_6$) for 10 minutes at 37°C in a total volume of 20 μL. Heparin, at a concentration of 100 μg/mL, was then added to the reaction followed by the addition of 2.5 μL of an NTP mixture (containing 500 μM of ATP, GTP, CTP, UTP, and 0.5 μL of [α-^{32}P]UTP) and 0.25 μL of RNase inhibitor. The reaction mixture was then incubated at 37°C for another 20 minutes. Following incubation, a mixture of 70 μL of water, 10 μL of 3M NaOAc (pH 5.2, adjusted with acetic acid), and 2 μL of 0.5 M EDTA was added to the reaction mixture. The RNA product was precipitated overnight at −20°C after the addition of 2 μL of glycogen blue and 330 μL of ethanol. RNA was re-suspended in 10 μL of 80% formamide, 1X TBE buffer, 10 mM EDTA, 0.05% SDS and 0.025% bromophenol blue and kept at 100°C for 2 minutes. RNA samples were loaded onto a 6% urea polyacrylamide gel and electrophoresed at 1000 V.

Fig. S1E shows the results of *in vitro* transcription assay. With WT RNAP but without CueR, some RNA product was detected (Fig. S1E, left), consistent with the well-known leakage transcription from the weakly repressed P*copA* promoter. In the presence of WT RNAP and holo CueR, much more RNA product was detected, reflecting the transcription activation (Fig. S1E, middle). In the presence of our labeled $RNAP_{Cy5}$ and holo-CueR, a comparable amount of RNA was detected (i.e., about ~73 ± 5%, which is in agreement with previously reported activity of σ^{70}_{R596C} at the *merTPAD* operon in the presence of holo-MerR (17)) to that using WT RNAP (Fig. S1E, right). Therefore, our labeled $RNAP_{Cy5}$, where Cy5 is attached to σ^{70}_{R596C}, is transcriptionally active, although slightly less active than the wild type RNAP.

In order to confirm that transcription could still occur on both of our labeled P*copA* strands, $P\mathit{copA}_{Cy3@-41}$ and $P\mathit{copA}_{Cy3@-5}$, the same transcription run-off assay was performed as described above using these two as templates with WT RNAP and holo-CueR. RNA products were detected in both cases, indicating that our two Cy3-labeled P*copA* templates are both functional templates (Fig. S1F).

f. Single-molecule FRET imaging and data analysis

The single-molecule FRET imaging experiments were performed at room temperature using a prism-type total internal reflection microscope, based on an Olympus IX71 inverted microscope, and the data were analyzed as previously described (14, 18). Briefly, immobilized Cy3-labeled DNA was excited directly by a continuous-wave circularly polarized 532-nm laser at ~4 mW over an area of ~150 × 75 μm^2. The Cy3 and Cy5 fluorescence was collected, split into two channels, projected onto two halves of an EMCCD camera, operated continuously at 30 ms time resolution. Individual Cy3 and Cy5 fluorescence intensity trajectories for proteins interacting with single immobilized DNA molecules were extracted from the recorded fluorescence movies using a custom IDL program. The E_{FRET} was approximated as $I_{Cy5}/(I_{Cy5}+I_{Cy3})$, where I_{Cy3} and I_{Cy5} are the fluorescence intensities. A forward-backward nonlinear filter was used to reduce the noise in the fluorescence trajectories (19-21). The E_{FRET} histograms were compiled from hundreds of trajectories at each condition. The E_0 peaks were fit with a Voigt

distribution while the E_{FRET} peaks from the various DNA-protein complexes were fit with Gaussian distributions. This was done in order to achieve the best fit.

A microfluidic channel formed by a quartz slide and a borosilicate cover slip fixed together using double-sided tape was used to contain the samples. Quartz slides were amine-functionalized with (3-Aminopropyl) triethoxysilane (Sigma-Aldrich) (22), followed by PEG coating (polyethylene glycol polymers) (Nanocs, 100 mg/mL m-PEG-SPA-5000 and 1 mg/mL biotin-PEG-NHS-3400) in order to minimize nonspecific protein/DNA adsorption on the quartz surface. A biotinylated terminal group, to form biotin-neutravidin linkages for immobilizing biotinylated DNA molecules, comprised one percent of the PEG polymers. A 500 µL solution of 0.2 mg/mL neutravidin (Invitrogen) was introduced to the microfluidic channel and incubated for 15 minutes. Any remaining non-functionalized quartz and borosilicate surfaces were blocked using 3 mL BSA (0.1 mg/ml). A 500 µL solution of 10 pM Cy3-labeled biotinylated P*copA* DNA in 50 mM Tris, 2 mM $MgCl_2$ buffer at pH 7.35 was flowed through the channel for immobilization. In imaging protein-DNA interactions, the labeled RNAP solutions of 2 to 5 nM or labeled CueR solutions of 0.5 to 10 nM were flowed continuously at a rate of 10 µL/min in a buffer containing 50 mM Tris (pH 7.35), 100 mM Potassium Glutamate, 1 mg/ml BSA, 2 mM $MgCl_2$, 1 mM $CaCl_2$, 2 mM DTT, 0.1 mM EDTA, 5% glycerol (2, 11, 23) and an oxygen scavenging system (1mM Trolox, 2.5 mM PCA, 50 nM PCD) (24). Depending on the experimental conditions, varying concentrations of unlabeled RNAP or unlabeled CueR were added accordingly.

2. RNAP-P*copA* complex population increases with [RNAP]

In E_{FRET} histogram of $RNAP_{Cy5}$–P$copA_{Cy3@-41}$ interactions, the three E_{FRET} states ($E_0 \sim 0.07$, $E_1 \sim 0.78$, and $E_2 \sim 0.95$) correspond to the free P*copA* (E_0) and two RNAP-P*copA* complexes (E_1, dead-end complex; and E_2, open complex) (Fig. S2A), as described in the main text (see Fig. 2D). Increasing $RNAP_{Cy5}$ concentration results in an increase of the relative populations of the two complexes relative to that of the free P*copA* state (Fig. S2B). On the other hand, the relative stabilities of the two complexes are independence of RNAP concentration, as expected as well (Fig. S2C)

The equilibrium constants for forming the RNAP-P*copA* complexes can be determined from the area ratios of the resolved peaks in the E_{FRET} histograms, as described by Eq [3] and Eq [4] in Section 11 later. From the $RNAP_{Cy5}$-P$copA_{Cy3@-41}$ data in Fig. S2A-B, the obtained dissociation constants are K_{1D} = 40 ± 3 nM and K_{2D} = 147 ± 11 nM, which are consistent with K_{1D} = 35 ± 5 nM and K_{2D} = 126 ± 17 nM, calculated from the rate constants (Table 1 in the main text) or K_{1D} = 30 ± 3 nM and K_{2D} = 105 ± 26 nM obtained from EFRET histogram analysis (Table S1) for $RNAP_{Cy5}$-P$copA_{Cy3@-5}$ interactions.

The overall formation constant K_A of RNAP-P*copA* complexes is:

$$K_A = \frac{[RP_{DE}]+[RP_O]}{[P][R]} \rightarrow K_A[R] = \frac{[RP_{DE}]+[RP_O]}{[P]} = \frac{(E_1+E_2)\text{ peak area}}{E_0\text{ peak area}} \qquad \text{Eq. [1]}$$

Fitting the $RNAP_{Cy5}$-P$copA_{Cy3@-41}$ data in Fig. S2B gives an overall formation constant $K_A \sim (32 \pm 2) \times 10^6\ M^{-1}$, corresponding to an overall dissociation constant of K_D = 31 ± 2 nM.

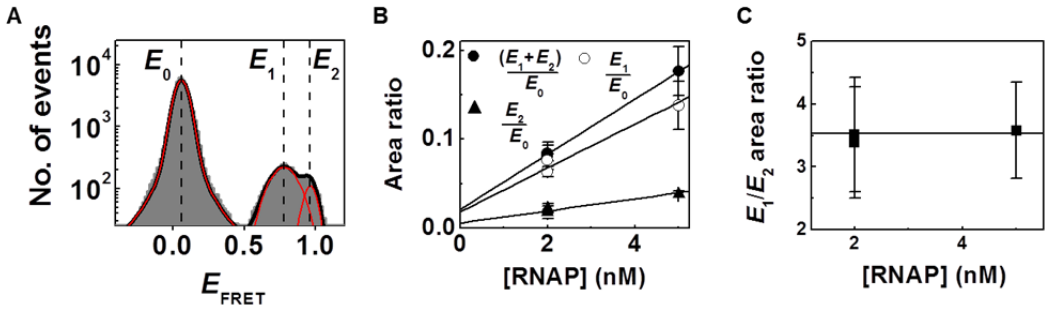

Fig. S2. RNAP–P*copA* interactions in the absence of CueR. (A) E_{FRET} histogram of $RNAP_{Cy5}$–P$copA_{Cy3@-41}$ interactions at 5 nM [RNAP]. Red lines are resolved peaks centered at E_{FRET} ~0.07, ~0.78, and ~0.95, with percentage areas of 85.0 ± 3.1%, 11.7 ± 1.8%, and 3.3 ± 0.3%, respectively. (B) [$RNAP_{Cy5}$] dependence of the $(E_2+E_1)/E_0$, E_1/E_0 and E_2/E_0 peak area ratios obtained from the E_{FRET} histograms as in A of $RNAP_{Cy5}$–P$copA_{Cy3@-41}$ or $RNAP_{Cy5}$–P$copA_{Cy3@-5}$ interactions. The solid lines are a linear fits with Eq [3] and Eq [4] from SI Section 11, and Eq. [1], respectively. Note that the data here have non-zero y-intercept, most likely an artifact of the E_{FRET} trajectory selection, because only trajectories that had 2 or more transitions between the FRET states were analyzed (trajectories without transitions are difficult to differentiate from nonspecifically adsorbed dye molecules), resulting in an apparent complex formation even at [RNAP] → 0. We thus added a *y*-offset when fitting the data. (C) E_1 and E_2 peak area ratios from E_{FRET} histograms with increasing [RNAP]. Solid line is a horizontal line at ~3.6.

3. RNAP does not form *specific* complexes with a nonspecific DNA lacking promoter recognition sequence.

As a control, we examined $RNAP_{Cy5}$ interactions with a Cy3-labeled 100 bp nonspecific DNA, which does not contain the promoter sequence. This nonspecific DNA was copied out from the *copA* gene, spanning from position +161 to +251, and was labeled with biotin-TEG at the 5′ end of the template strand and labeled with Cy3 19 bp in from the 5′ end of the nontemplate strand (same distance from the 5' end as in P$copA_{Cy3@-41}$) (Fig. S3A).

Fig. S3B shows a single-molecule E_{FRET} trajectory of this nonspecific DNA interacting with $RNAP_{Cy5}$ at 2 nM in solution. RNAP binding to this nonspecific DNA was observed, reflected by the E_{FRET} states higher than the free DNA state at E_{FRET} ~ 0.07. This binding is expected, as RNAP is known to interact with nonspecific DNA as well and with weaker affinity. However, as this DNA does not contain the −10 and −35 elements, RNAP's binding can occur anywhere along the DNA length. This nonspecific binding is reflected in the E_{FRET} histogram: aside from the dominant peak at ~0.07 from the free DNA state, the higher E_{FRET} values are spread over the range of ~0.4 to 1 without a distinct peak (Fig. S3C), in contrast to $RNAP_{Cy5}$ –P$copA_{Cy3@-41}$ interactions for which distinct higher E_{FRET} states are clear (Fig. S3C).

Using the population ratio of bound vs. unbound states, we estimated the dissociation constant K_D to be about 1.1 ± 0.4 μM, consistent with reported dissociation constants of RNAP interacting with non-promoter DNA (K_D ~ 10^{-3} M to 10^{-6} M, depending on the solution salt concentrations) (25-28). Therefore, holo RNAP can interact with nonspecific DNA with weaker affinity, but does not form specific complexes.

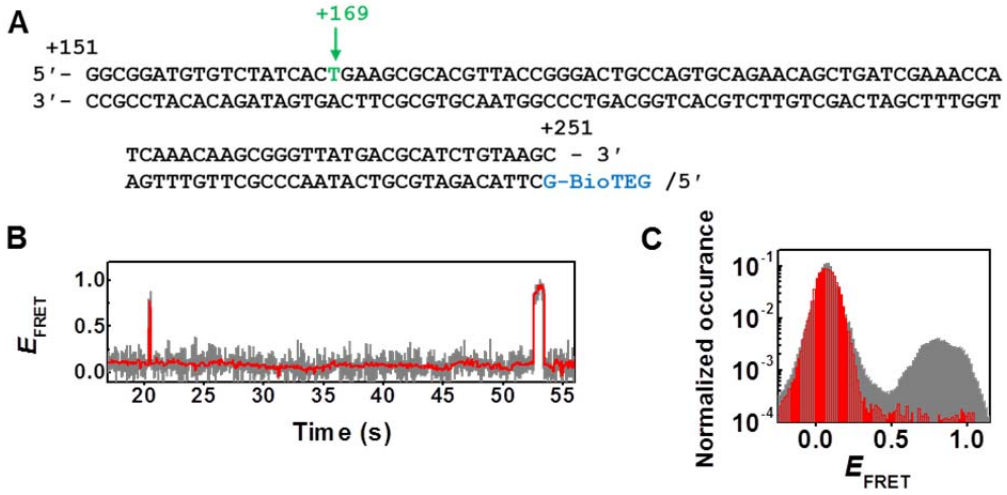

Fig. S3. RNAP interactions with nonspecific DNA. (A) Sequence of the nonspecific Cy3 labeled DNA, copied from the *copA* gene spanning from +161 to +251 position. The Cy3 dye is attached at +169 position (green vertical arrow) via an amine modified T (denoted in green). The Biotin-TEG is attached to the 5'-end of the template strand (shown in blue) for immobilization. (B) Single-molecule E_{FRET} trajectory of immobilized nonspecific Cy3 labeled DNA interacting with 2 nM $RNAP_{Cy5}$. The grey line is original data; the red line is after non-linear filtering. (C) Normalized E_{RRET} histogram of $RNAP_{Cy5}$ interactions with the nonspecific Cy3 labeled DNA (red); [$RNAP_{Cy5}$] = 2 nM. Superimposed is the normalized E_{FRET} histogram of $RNAP_{Cy5}$–P*copA*$_{Cy3@-41}$ interactions (grey, from Fig. 2D in the main text).

4. The shift of RNAP-P*copA* interactions toward the initial minor open complex, caused by holo-CueR, is proportional to [holo-CueR]

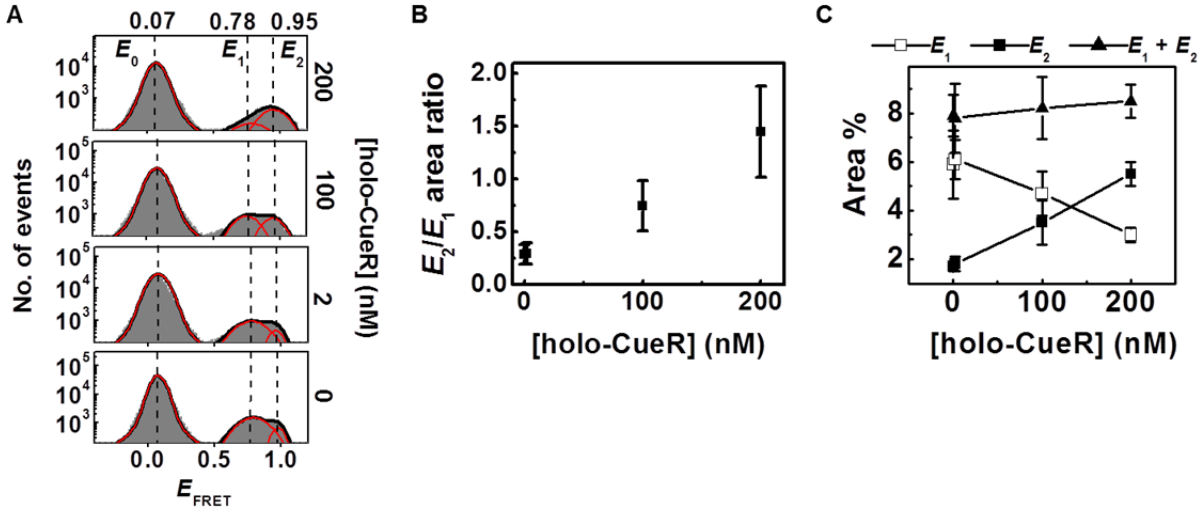

Fig. S4. The shift of RNAP-P*copA* interactions toward the initial minor open complex, caused by holo-CueR, is proportional to the [holo-CueR]. (A) E_{FRET} histograms of P*copA*$_{Cy3@-41}$ interacting with 2 nM $RNAP_{Cy5}$ in the absence or presence of varying concentrations of unlabeled holo-CueR. The maximum concentration (200 nM) of holo-CueR used here is well above the previously determined K_D (~ 122 ± 63 nM) for holo-CueR binding to P*copA* (14). (B) E_2/E_1 area ratio vs. [holo-CueR] from A, **showing the population shift toward the E_2 complex (i.e., open complex) is proportional to [holo-CueR]**. (C) Absolute area percent of E_1, E_2 and $E_1 + E_2$ vs. [holo-CueR] from A, showing that this population shift results from the continuous stabilization of the open complex (E_2) and the destabilization of the

dead-end closed-like complex (E_1), and the overall RNAP-P*copA* complexes (E_1 + E_2) are stabilized slightly.

5. In the presence of holo-CueR, ATP further stabilizes the RNAP–P*copA* open complex; by itself, it has no effect; and in the presence of apo-CueR, it exerts no effect on RNAP–P*copA* interactions either.

a. In the presence of the activator holo-CueR, addition of the initiating nucleotide ATP further stabilizes slightly the RNAP-PcopA open complex while destabilizing slightly the dead-end complex

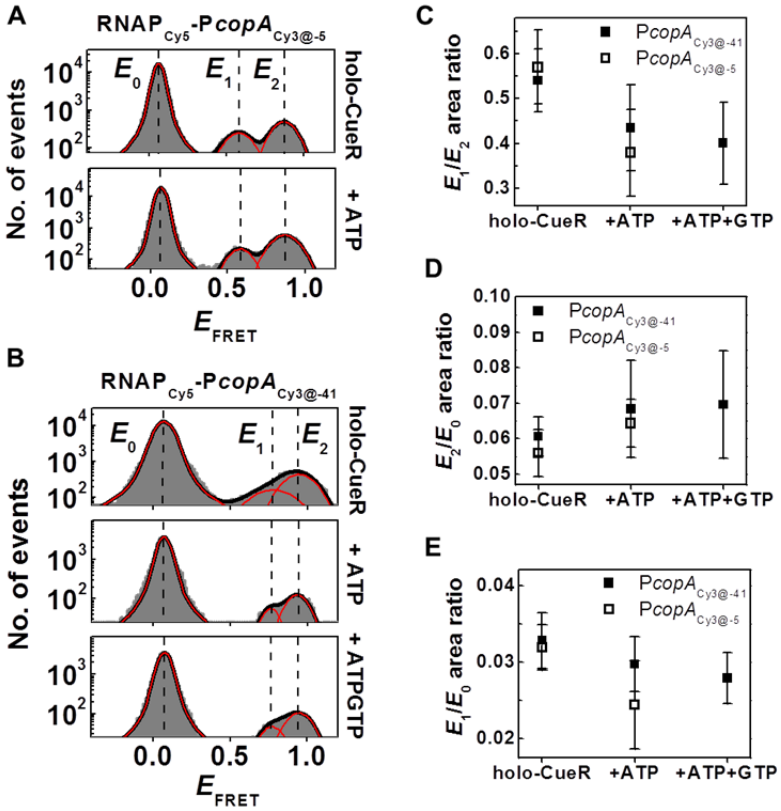

Fig. S5. In the presence of the activator holo-CueR, addition of the initiating nucleotide ATP further stabilizes slightly the RNAP-P*copA* open complex while destabilizing slightly the dead-end complex. (A) E_{FRET} histograms of $RNAP_{Cy5}$–P$copA_{Cy3@-5}$ interactions at 2 nM RNAP in the presence of 200 nM holo-CueR (top panel, same as Fig. 4A in the main text) or of 200 nM holo-CueR and 1 mM ATP (bottom panel). In each panel, the resolved peaks center at E_{FRET} ~0.07, ~0.58, and ~0.87. (B) E_{FRET} histograms of $RNAP_{Cy5}$–P$copA_{Cy3@-41}$ interactions at 2 nM RNAP in the presence of 200 nM holo-CueR (top panel), or of 200 nM holo-CueR and 1 mM ATP (middle panel), or of 200 nM holo-CueR, 1 mM ATP and 1 mM GTP (bottom). In each panel, the resolved three peaks center at E_{FRET} ~0.07, 0.78, and ~0.95. (C-E) E_1/E_2 (C), E_2/E_0 (D), and E_1/E_0 (E) area ratios from A-B. These area ratios show that the addition of the initiating nucleotide ATP further shifts the RNAP-P*copA* interaction complexes toward the E_2 open complex (C), and this shift is from both further stabilization of the E_2 open complex (D) and further destabilization of the E_1 dead-end complex (E) relative to the E_0 free P*copA* form. Further addition of the next nucleotide, GTP, does not cause any discernable changes (C-E). Part of data in (C) are presented in Fig. 4A in the main text.

b. No discernable change is observed in RNAP-PcopA interactions with the addition of ATP only

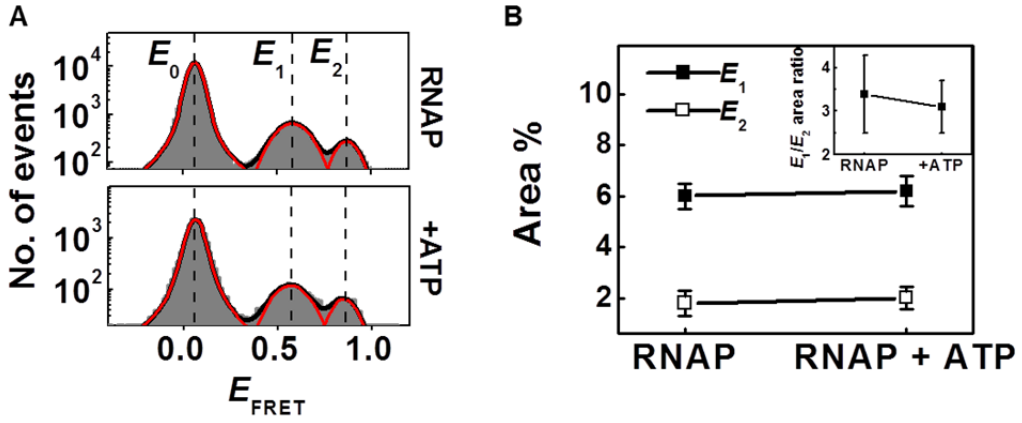

Fig. S6. No discernable change is observed in RNAP-P*copA* interactions with the addition of ATP only. (A) E_{FRET} histogram of $RNAP_{Cy5}$–P*copA*$_{Cy3@-5}$ interactions at 2 nM [RNAP] (top panel, same as Fig. 2C in the main text) and in the presence of 1 mM ATP (bottom panel). Resolved peaks center at E_{FRET} ~0.07, ~0.58, and ~0.87. (B) Area percent of E_1 and E_2 from A. Inset: E_1/E_2 area ratio from A. These data show no discernable change in the relative stabilities of the two RNAP-P*copA* complexes, as reported by the relative peak areas.

c. Apo-CueR reinforces the dead-end RNAP-PcopA complex, and addition of the initiating nucleotide ATP has no additional effect on the formed RNAP–PcopA complexes

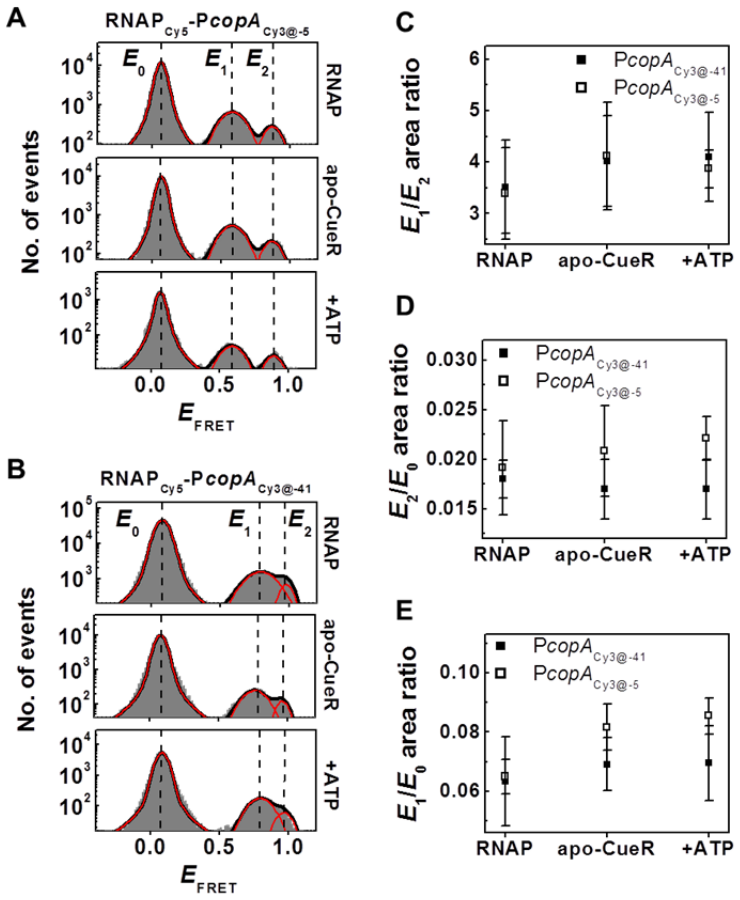

Fig. S7. Apo-CueR reinforces the dead-end RNAP-P*copA* complex, and addition of the initiating nucleotide ATP has no additional effect on the formed RNAP–P*copA* complexes. (A) E_{FRET} histograms of RNAP$_{Cy5}$–P*copA*$_{Cy3@-5}$ interactions at 2 nM RNAP$_{Cy5}$ only (duplicate of main text Fig. 2C), or further in the presence of 200 nM apo-CueR (duplicate of main text Fig. 4B) or of 200 nM apo-CueR and 1 mM ATP. Resolved peaks center at E_{FRET} ~0.07, ~0.58, and ~0.87. (B) Same as A, but with P*copA*$_{Cy3@-41}$. Resolved peaks center at ~0.07, ~0.78, and ~0.95. (C-E) Area ratio of E_1/E_2, E_2/E_0, and E_1/E_0 obtained from the E_{FRET} histograms in (A) and (B). These area ratios show that the apo-CueR reinforces RNAP-P*copA* interactions toward the E_1 dead-end complex (C); the reinforcement comes from the slight stabilization of the E_1 dead-end complex relative to the E_0 free P*copA* state (E), while the stability of the E_2 open complex increases slightly (change is very small here). Further addition of ATP does not cause significant changes (C-E). Part of data in (C) are presented in Fig. 4B in the main text.

6. RNAP can bind to apo-CueR-P*copA* complex

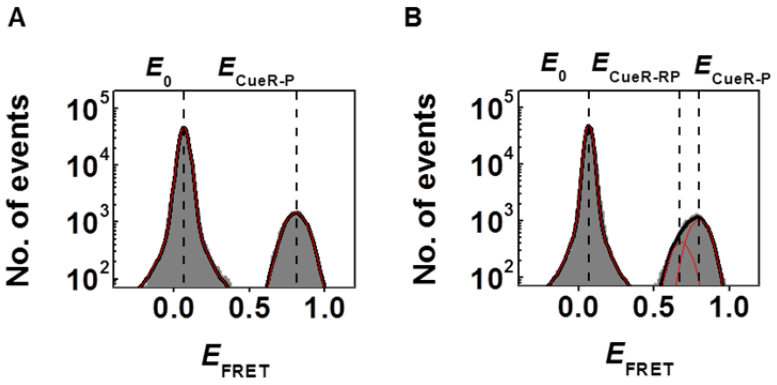

Fig. S8. RNAP can bind to apo-CueR–P*copA* complex. (A) E_{FRET} histogram of apo-$CueR_{Cy5}$ –P$copA_{Cy3@-41}$ interactions at 10 nM apo-$CueR_{Cy5}$. Resolved peaks center at E_0 ~0.07 and E_{CueR-P} ~0.81, with percentage peak areas of 93.8 ± 6.1% and 6.2 ± 2.6%, respectively. (B) Same as A, but with 5 nM unlabeled RNAP. Resolved peaks center at E_0 ~0.07, $E_{CueR-RP}$ ~0.68, and E_{CueR-P}~0.81, with percentage peak areas of 92.7 ± 1.8%, 5.3 ± 0.9%, and 2.0 ± 0.6%, respectively. The peak $E_{CueR-RP}$ ~0.68 is from a ternary RNAP-(apo-CueR)-P*copA* complex, similar to the case of RNAP binding to holo-CueR-P*copA* complex in Fig. 5 in the main text.

7. $E_{CueR-RP}$ peak of the ternary RNAP-(holo-CueR)-P*copA* complex increases in population while the E_{CueR-P} peak of the holo-CueR-P*copA* complex decreases with increasing [RNAP]

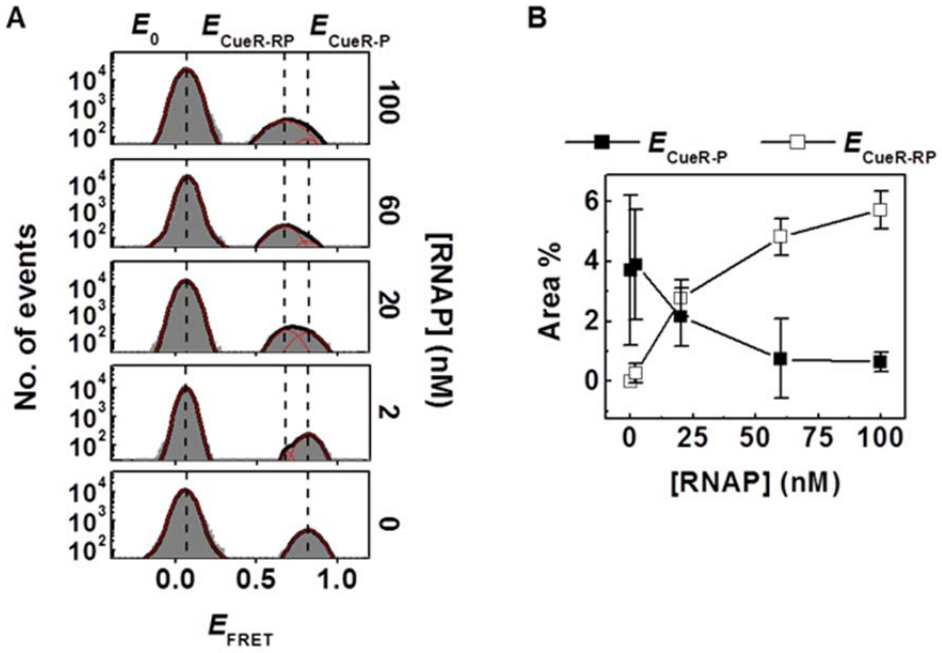

Fig. S9. RNAP binding effects on holo-$CueR_{Cy5@C129}$–P$copA_{Cy3@–41}$ interactions. (A) E_{FRET} histograms of P$copA_{Cy3@-41}$ interactions with 2 nM holo-$CueR_{Cy5@C129}$ in the absence and presence of unlabeled RNAP at 2, 20, 60, and 100 nM. Resolved peaks center at E_{FRET} ~0.07 (E_0 state), ~0.68 ($E_{CueR-RP}$ state), and ~0.81 (E_{CueR-P} state). The 0 nM and 100 nM RNAP panels are duplicated from main text Fig. 5A and B. (B) Area percent of E_{CueR-P} and $E_{CueR-RP}$ states from A. These data show that the $E_{CueR-RP}$ state increases in population while the E_{CueR-P} state decreases in population with increasing [RNAP], as well as that RNAP can bind to the holo-CueR-DNA complex to form a ternary complex comprised of RNAP, P*copA* and CueR.

8. In the absence of σ^{70}, the core RNAP does not bind to the (holo) CueR-P*copA* complex

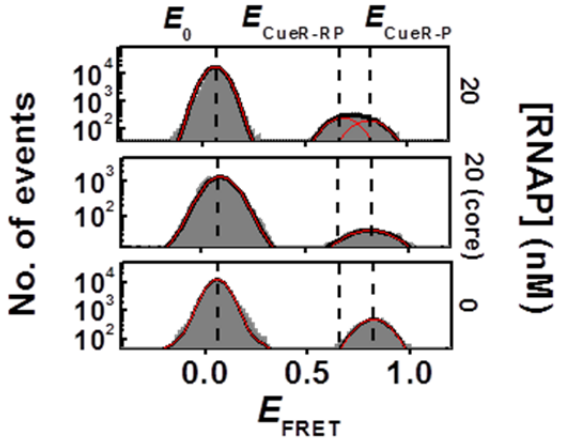

Fig. S10. The core RNAP does not bind to the (holo) CueR-P*copA* complex. E_{FRET} histograms of P*copA*$_{Cy3@-41}$ interactions with 2 nM holo-CueR$_{Cy5}$ in the absence (bottom panel, reproduced from Fig. 5A) or presence of 20 nM holo RNAP (top, reproduced from Fig. S9A) or 20 nM core RNAP (middle). The ternary RNAP-CueR-P*copA* complex at $E_{CueR-RP}$ ~0.68 does not appear in the presence of core RNAP only.

9. RNAP locks CueR into the specific binding mode on P*copA*.

a. Background: CueR has two binding modes on specific DNA (e.g., PcopA), one specific and the other nonspecific binding mode; and at the specific binding mode, CueR can undergo assisted dissociation and direct substitution on DNA.

Our previous smFRET studies of CueR$_{Cy5}$-DNA$_{Cy3}$ interactions showed that CueR, in both holo and apo forms, can bind to a specific DNA with two different binding modes: one in which CueR recognizes its specific dyad symmetric sequence and distorts the DNA structure (**I** in Fig. S11) and the other in which CueR likely interacts with the DNA in a nonspecific fashion (**I'** in Fig. S11) (14). These two different binding modes do not have resolvable differences in their E_{FRET} values, and their presences are experimentally manifested by the distribution of dwell time (τ_{bound}) of CueR at the bound state: this distribution follows a double-exponential decay behavior (e.g., Fig. 5C in the main text for the dwell-time distribution of the holo-CueR$_{Cy5}$–P*copA*$_{Cy3@-41}$ complex), instead of a single exponential distribution typically seen for a protein-DNA complex with a single binding mode.

At the specific binding mode, both holo- and apo-CueR can undergo assisted dissociation and direct substitution processes (Fig. S11). In the assisted dissociation process, an incoming CueR from solution helps carry away the incumbent CueR bound on DNA; in the direct substitution reaction, the incoming protein directly replaces the incumbent one on DNA. A characteristic experimental signature of these two processes is the dependence on CueR concentration of the average dwell time $\langle\tau_{bound}\rangle$ on the bound CueR-DNA state. With increasing [CueR], $\langle\tau_{bound}\rangle^{-1}$ increases linearly, because both the assisted dissociation and direct substitution disrupt the existing CueR-DNA complex, making the dwell time of the incumbent protein on DNA shorter.

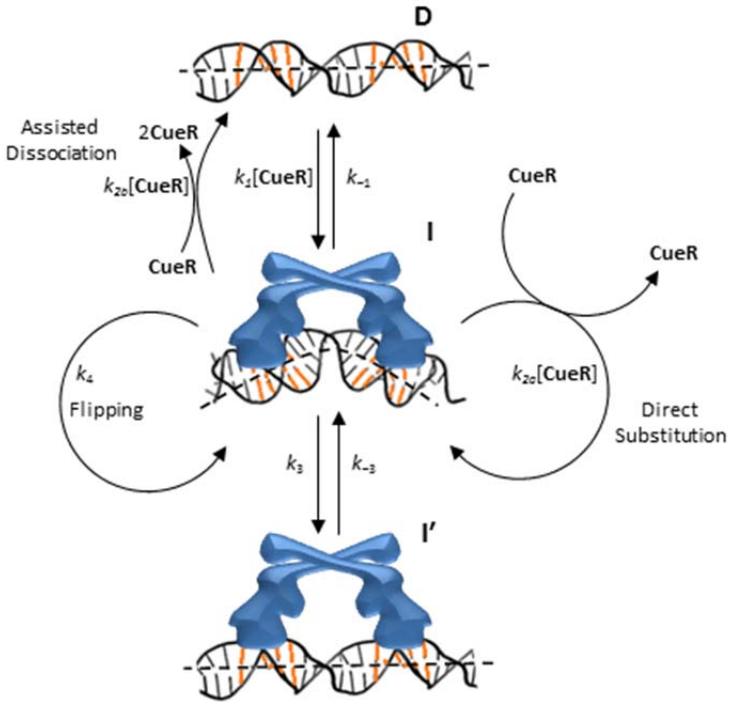

Fig. S11. The kinetic mechanism of CueR interacting with a specific DNA from reference (14), where the free DNA is designated as D and [CueR] stands for CueR concentration. CueR binds to DNA reversibly, where k_1 and k_{-1} correspond to the binding and unbinding kinetic rate constants, respectively. CueR has two different binding modes on DNA: one in which CueR recognizes the promoter sequence and distorts the DNA structure (designated as I, the specific binding mode) and the other where CueR interacts with DNA in a nonspecific fashion (designated as I′), and they can interconvert (k_3 and k_{-3}). CueR can undergo flipping (k_4) on DNA at the specific binding mode, where the protein flips its binding orientation spontaneously without detaching from DNA completely. CueR can also undergo direct substitution (k_{2a}), where an incoming protein replaces the incumbent CueR on DNA to form a new CueR-DNA complex, or assisted dissociation (k_{2b}), where an incoming protein carries away the incumbent CueR, leading to free DNA.

b. In the presence of RNAP, the assisted dissociation and/or direct substitution processes of CueR on PcopA still occur, indicating that the specific binding mode of CueR on PcopA persists.

Here we also examined the [CueR] dependence of CueR's dwell time on P*copA* in the presence of RNAP by studying holo-$CueR_{Cy5}$–P*copA*$_{Cy3@-41}$ interactions. In the presence of RNAP, the E_{FRET} histogram can be resolved to have two bound CueR-DNA state, $E_{CueR\text{-}P}$ and $E_{CueR\text{-}RP}$, where the $E_{CueR\text{-}RP}$ state is a ternary RNAP-CueR-P*copA* complex, as we discussed in the main text (Fig. 5B). In the E_{FRET} vs time trajectory, the dwell time on the $E_{CueR\text{-}P}$ and $E_{CueR\text{-}RP}$ states are difficult to separate (Fig. S12A). We thus combine them together, referring to the residence time as τ_{bound}. Fig. S12B shows that in the presence of RNAP, $\langle \tau_{bound} \rangle^{-1}$ still shows a linear dependence on [holo-$CueR_{Cy5}$]. Therefore, in the presence of RNAP, the assisted dissociation and direct substitution processes still occur to CueR bound on P*copA*.

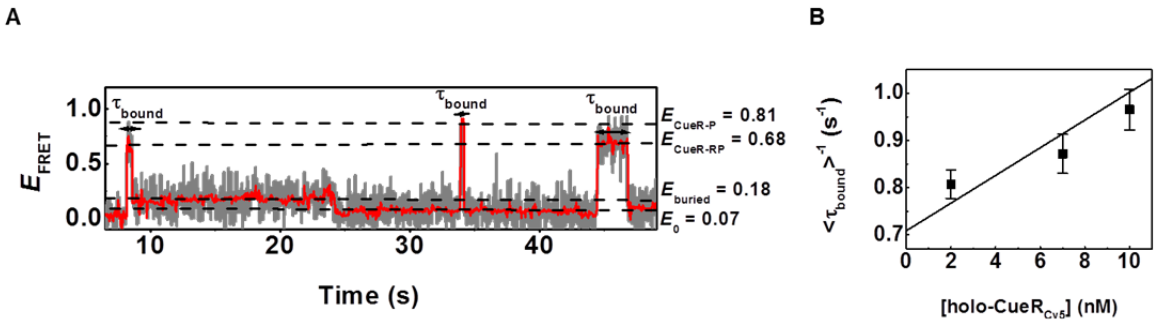

Fig. S12. Dependence of τ_{bound}, CueR's dwell time on P*copA*, on [CueR] in the presence of RNAP. (A) Single-molecule E_{FRET} trajectory of immobilized P*copA*$_{Cy3@-41}$ interacting with 2 nM holo-CueR$_{Cy5}$ in the presence of 20 nM RNAP. The grey line is original data; the red line is after non-linear filtering. τ_{bound} designates the dwell times on the E_{CueR-P} or $E_{CueR-RP}$ state. The E_{buried} = 0.18 state is the other CueR binding orientation on P*copA*, where the acceptor on one of the CueR monomers is further away from the donor on P*copA*. This E_{buried} state is not resolved in the E_{FRET} histogram in Fig. 5A and B in the main text. (B) Dependence of $\langle \tau_{bound} \rangle^{-1}$ on [CueR] for holo-CueR$_{Cy5}$–P*copA*$_{Cy3@-41}$ interactions in the presence of 5 nM [RNAP]. Solid line is a linear fit.

c. Simulations show that the dominance of the specific binding mode will lead to a single-exponential distribution of dwell time distribution, supporting that RNAP locks CueR binding to PcopA into its specific binding mode.

In the absence of RNAP, the distribution of dwell time τ_{bound} for holo-CueR$_{Cy5}$–P*copA*$_{Cy3@-41}$ interactions shows a double-exponential decay behavior (Fig. 5C in the main text), reflecting the two binding modes of CueR on P*copA*, as we showed previously (14). With the addition of RNAP, the distribution of τ_{bound} follows a single-exponential decay (Fig 5D), suggesting that the CueR-bound state is now dominated by one binding mode, while the other binding mode becomes insignificant. On the other hand, in the presence of RNAP, the assisted dissociation and/or direct substitution processes of CueR still exist on P*copA* (Fig. S12, and Section 9b above). As these two processes only occur to CueR's specific binding mode, we conclude that the remaining dominant binding mode is the specific mode; in other words, RNAP interactions locks CueR into its specific binding mode on P*copA*.

To support that the dominance of the specific binding mode is indeed associated with the conversion of the double-exponential distribution of dwell time into a single-exponential distribution, we performed simulations of the dwell time distribution from the kinetic mechanism in Fig. S11. In this mechanism, the distribution of the dwell time on the CueR-bound state (on each of its binding orientations) follows:

$$f_{bound}(\tau)=\frac{D}{4M}\left[(M+C)\exp\left\{-\frac{(N-2M)\tau}{4}\right\}+(M-C)\exp\left\{-\frac{N\tau}{4}\right\}\right] \qquad \text{Eq. S[2]}$$

Here $M=\sqrt{\left[2k_{-3}+2k_{-1}+2k_3+2k_4+k_{2a}[\text{CueR}]\right]^2-8k_{-3}\left[2k_{-1}+2k_4+k_{2a}[\text{CueR}]\right]}$,

$N=M+2\left(k_{-3}+k_{-1}+k_3+k_4\right)+k_{2a}[\text{CueR}]$, $C=\left[2\left(k_{-3}-k_{-1}-k_3-k_4\right)-k_{2a}[\text{CueR}]\right]$, and $D=\left[2\left(k_{-1}+k_4\right)+k_{2a}[\text{CueR}]\right]$, as we previously derived (14); [CueR] is CueR concentration. This distribution is a double exponential decay function, as shown in Fig. S13A using kinetic rate constants determined from our previous studies (14). To make the specific binding mode (**I** in Fig. S11) dominate the bound state, we performed the following:

(1) Make the rate constants k_3 and k_{-3} both zero, thus effectively eliminating the nonspecific binding mode (**I'** in Fig. S11).
(2) Make $k_3 << k_{-3}$, thus biasing the equilibrium toward the specific binding mode, making it dominant.

In both cases, the simulated dwell time distributions converts to a single-exponential decay behavior (Fig. S13A for case (1) and B for case (2)), thus supporting that this distribution is consistent with that RNAP locks CueR's interactions with P*copA* into its specific binding mode.

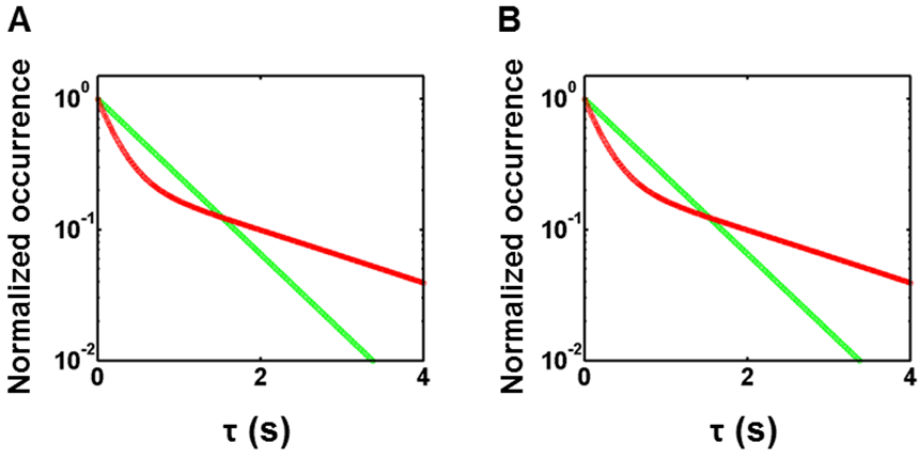

Fig. S13. (A) Red: normalized distribution of τ_{bound} for holo-CueR$_{Cy5}$–DNA$_{Cy3}$ at 2 nM holo-CueR using equation Eq. S[2] and k_{-1} = 1.1 s^{-1}, k_{2a} = 134 x 10^6 M^{-1} s^{-1}, k_4 = 0.13 s^{-1}, k_3 = 2.0 s^{-1} and k_{-3} = 1.4 s^{-1} from our previous studies of CueR (14). Green: same as red, but with k_3 = 0 s^{-1} and k_{-3} = 0 s^{-1}. (B) Red, same as the red curve in A. Green: same as red but with k_3 = 1 s^{-1} and k_{-3} = 1000 s^{-1}.

10. CueR increases the overall affinity of RNAP to P*copA*, and RNAP also increases the overall affinity of CueR to P*copA*, reflecting their synergistic interactions

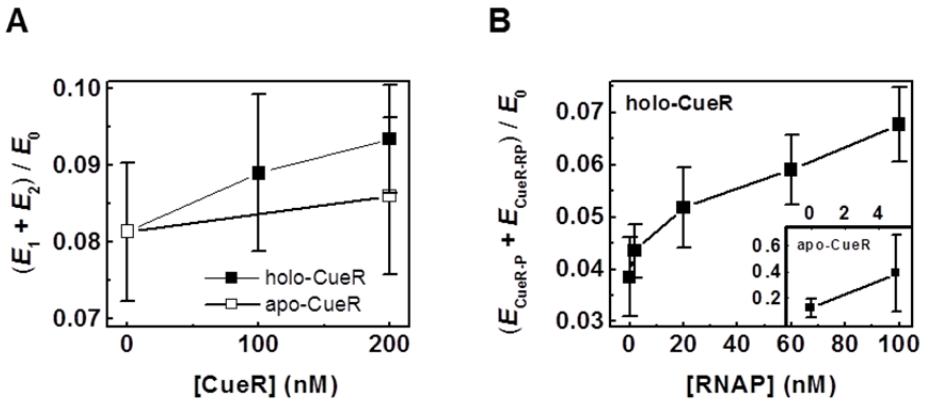

Fig. S14. RNAP and CueR increase each other's overall affinity to P*copA*. (A) Area ratio of $(E_1+E_2)/E_0$ obtained from the E_{FRET} histograms of RNAP$_{Cy5}$-P*copA*$_{Cy3@-41}$ interactions in Fig. S4A in the presence of holo-CueR and from those in Fig. S7B in the presence of apo-CueR. The data here show that the overall RNAP-P*copA* affinity, represented by the combined populations of the E_1 and E_2 complexes relative to the free P*copA* state E_0, increases in the presence of holo-CueR or apo-CueR, by up to ~15% at 200 nM CueR. (B) Area ratio of $(E_{CueR-P}+E_{CueR-RP})/E_0$ obtained from the E_{FRET} histograms of holo-CueR$_{Cy5}$-P*copA*$_{Cy3@-41}$

interactions in Fig. S9A in the presence of RNAP. Inset: Area ratio of ($E_{CueR\text{-}P}$+$E_{CueR\text{-}RP}$)/E_0 obtained from the E_{FRET} histograms of apo-CueR$_{Cy5}$-P*copA*$_{Cy3@-41}$ interactions in Fig. S8A and B in the presence of RNAP. Note: the area of the buried $E_{CueR\text{-}P}$ and $E_{CueR\text{-}RP}$ peaks have been subtracted from the E_0 peak area and added to the unburied $E_{CueR\text{-}P}$ and $E_{CueR\text{-}RP}$ peak areas to account for both orientations of labeled CueR on P*copA*. The data here show that the overall holo- or apo-CueR-P*copA* affinity increases in the presence of RNAP, by up to ~70% at 100 nM RNAP.

11. Thermodynamic equilibrium cycle analysis results in dissociation constants that further support the synergistic effects of RNAP and CueR interactions with P*copA*.

Fig. S15 shows a simplified equilibrium cycle of interactions between CueR, RNAP (i.e., **R**), and P*copA* (i.e., **P**). The cycle includes CueR-P*copA* interactions, RNAP-P*copA* interactions forming the open or dead-end complex, and ternary CueR-RNAP-P*copA* complexes that stabilize the open or the dead-end complex. For simplification, this cycle omits that CueR can bind to P*copA* in two different binding modes (i.e., the specific and nonspecific binding modes) and that CueR can undertake assisted dissociation and direct substation processes on P*copA*.

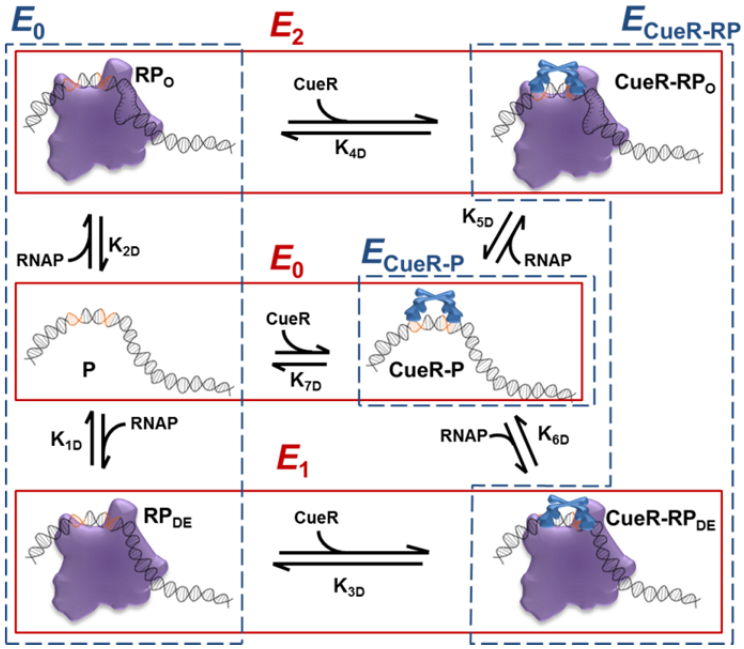

Fig. S15. The schematic diagram of a simplified overall CueR-RNAP-P*copA* interactions. The red boxes outline the species observed in smFRET measurements using Cy5-labeled RNAP, where E_2 is the E_{FRET} value for the open RNAP-P*copA* complex without CueR bound (designated **RP$_O$**) and with CueR bound (designated **CueR-RP$_O$**), E_1 is for the dead-end RNAP-P*copA* complex without CueR bound (designated **RP$_{DE}$**) and with CueR bound (designated **CueR-RP$_{DE}$**), and E_0 is for P*copA* without a bound RNAP (designated as **P** and **CueR-P**). The blue boxes outline the species observed in the smFRET measurements using Cy5-labeled CueR, where the E_0 represents the DNA species without a bound CueR (designated as **P**, **RP$_O$** and **RP$_{DE}$**), $E_{CueR\text{-}RP}$ represents the CueR-RNAP-P*copA* complexes that could be an open or dead-end complex (designated as **CueR-RP$_O$** and **CueR-RP$_{DE}$**), and $E_{CueR\text{-}P}$ represents the CueR-P*copA* complex (designated as **CueR-P**).

This simplified equilibrium cycle allows for thermodynamic analysis of the population ratios of different species from the resolved E_{FRET} histograms of RNAP$_{Cy5}$–P*copA*$_{Cy3}$ interactions and

$CueR_{Cy5}$–P*copA*$_{Cy3}$ interactions in the presence and absence of the other protein. The associated formation (K_A) and dissociation (K_D) equilibrium constants are defined as:

K_{1A} and K_{1D}: RNAP binding to P*copA* to form the dead-end closed-like complex

$$K_{1A} = \frac{1}{K_{1D}} = \frac{[RP_{DE}]}{[P][R]} \quad \text{Eq. [3]}$$

K_{2A} and K_{2D}: RNAP binding to P*copA* to form the open complex

$$K_{2A} = \frac{1}{K_{2D}} = \frac{[RP_O]}{[P][R]} \quad \text{Eq. [4]}$$

K_{3A} and K_{3D}: CueR binding to the dead-end RNAP-P*copA* complex

$$K_{3A} = \frac{1}{K_{3D}} = \frac{[\text{CueR-}RP_{DE}]}{[RP_{DE}][CueR]} \quad \text{Eq. [5]}$$

K_{4A} and K_{4D}: CueR binding to the open RNAP-P*copA* complex

$$K_{4A} = \frac{1}{K_{4D}} = \frac{[\text{CueR-}RP_O]}{[RP_O][CueR]} \quad \text{Eq. [6]}$$

K_{5A} and K_{5D}: RNAP binding to the CueR-DNA complex to form a ternary open complex

$$K_{5A} = \frac{1}{K_{5D}} = \frac{[\text{CueR-}RP_O]}{[\text{CueR-P}][R]} \quad \text{Eq. [7]}$$

K_{6A} and K_{6D}: RNAP binding to the CueR-DNA complex to form a ternary dead-end complex

$$K_{6A} = \frac{1}{K_{6D}} = \frac{[\text{CueR-}RP_{DE}]}{[\text{CueR-P}][R]} \quad \text{Eq. [8]}$$

K_{7A} and K_{7D}: CueR binding to P*copA*

$$K_{7A} = \frac{1}{K_{7D}} = \frac{[\text{CueR-P}]}{[P][CueR]} \quad \text{Eq. [9]}$$

In the E_{FRET} histograms from $RNAP_{Cy5}$–P*copA*$_{Cy3}$ interactions in the absence or presence of unlabeled CueR:

$$\frac{E_2}{E_0}\text{area ratio} = \frac{[RP_O]+[\text{CueR-}RP_O]}{[P]+[\text{CueR-P}]} = \frac{[RP_O]+K_{4A}[RP_O][CueR]}{[P]+K_{7A}[P][CueR]}$$
$$= \frac{[RP_O]}{[P]}\frac{(1+K_{4A}[CueR])}{(1+K_{7A}[CueR])} = K_{2A}[R]\frac{(1+K_{4A}[CueR])}{(1+K_{7A}[CueR])} \quad \text{Eq. [10]}$$

Equation [10] can be used for solving for K_{4A} (and subsequently K_{4D}) when K_{2A} and K_{7A} are known.

$$\frac{E_1}{E_0}\text{area ratio} = \frac{[RP_{DE}]+[\text{CueR-}RP_{DE}]}{[P]+[\text{CueR-P}]} = \frac{[RP_{DE}]+K_{3A}[RP_{DE}][CueR]}{[P]+K_{7A}[P][CueR]}$$
$$= \frac{[RP_{DE}]}{[P]}\frac{(1+K_{3A}[CueR])}{(1+K_{7A}[CueR])} = K_{1A}[R]\frac{(1+K_{3A}[CueR])}{(1+K_{7A}[CueR])} \quad \text{Eq. [11]}$$

Equation [11] can be used for solving for K_{3A} (and subsequently K_{3D}) when K_{1A} and K_{7A} are known.

$$\frac{E_2}{E_1}\text{ area ratio} = \frac{[\text{RP}_\text{O}]+[\text{CueR-RP}_\text{O}]}{[\text{RP}_\text{DE}]+[\text{CueR-RP}_\text{DE}]} = \frac{K_{2\text{A}}[\text{P}][\text{R}]+K_{5\text{A}}[\text{CueR-P}][\text{R}]}{K_{1\text{A}}[\text{P}][\text{R}]+K_{6\text{A}}[\text{CueR-P}][\text{R}]}$$
$$= \frac{K_{2\text{A}}[\text{P}][\text{R}]+K_{5\text{A}}K_{7\text{A}}[\text{P}][\text{R}][\text{CueR}]}{K_{1\text{A}}[\text{P}][\text{R}]+K_{6\text{A}}K_{7\text{A}}[\text{P}][\text{R}][\text{CueR}]} = \frac{K_{2\text{A}}+K_{5\text{A}}K_{7\text{A}}[\text{CueR}]}{K_{1\text{A}}+K_{6\text{A}}K_{7\text{A}}[\text{CueR}]} \qquad \text{Eq. [12]}$$

Equation [12] can be used for solving for $K_{5\text{A}}$ (and subsequently $K_{5\text{D}}$) when $K_{1\text{A}}$, $K_{2\text{A}}$, $K_{6\text{A}}$, and $K_{7\text{A}}$ are known.

In the E_{FRET} histogram of CueR_{Cy5}-P*copA*$_{\text{Cy3}}$ interactions in the absence or presence of unlabeled RNAP:

$$\frac{E_{\text{CueR-RP}}}{E_{\text{CueR-P}}}\text{ area ratio} = \frac{[\text{CueR-RP}_\text{O}]+[\text{CueR-RP}_\text{DE}]}{[\text{CueR-P}]} = \frac{K_{5\text{A}}[\text{CueR-P}][\text{R}]+K_{6\text{A}}[\text{CueR-P}][\text{R}]}{[\text{CueR-P}]} \qquad \text{Eq. [13]}$$
$$= K_{5\text{A}}[\text{R}]+K_{6\text{A}}[\text{R}] = [\text{R}](K_{5\text{A}}+K_{6\text{A}})$$

Equation [13] can be used for solving for $K_{6\text{A}}$ (and subsequently $K_{6\text{D}}$) when $K_{5\text{A}}$ is known.

Combining the above equations and earlier analysis, we could deduce all the thermodynamic equilibrium constants (e.g., dissociation constants), as summarized in Table S1. Note that the values of $K_{7\text{D}}$ for both holo- and apo-CueR interacting with P*copA* are in agreement with our previously determined dissociation constants for CueR binding to a specific DNA (14).

More important, these dissociation constants directly demonstrate the synergistic effects of RNAP and CueR binding to P*copA*, i.e., one protein's binding to P*copA* increases the binding affinity of the other protein to P*copA*. For example, the dissociation constants for RNAP-P*copA* dead-end and open complexes are $K_{1\text{D}}$ (RP_{DE}) ~ 30 nM and $K_{2\text{D}}$ (RP_O) ~ 105 nM, respectively. When holo-CueR is bound at P*copA*, RNAP binding to the holo-CueR-P*copA* complex to form the dead-end and open complexes have smaller dissociation constants, at $K_{5\text{D}}$ ($\text{CueR-RP}_{\text{DE}}$) ~ 29 nM and $K_{6\text{D}}$ (Cue-RP_O) ~ 34 nM, demonstrating that the bound holo-CueR enhances the affinity of the subsequent RNAP binding. Similar enhancement by apo-CueR to RNAP binding to P*copA* is also observed.

When RNAP is bound at P*copA*, it also enhances the subsequent CueR binding to the RNAP-P*copA* complexes. For example, the dissociation constant for holo-CueR binding to P*copA* is $K_{7\text{D}}$ (CueR-P) ~ 52 nM, and holo-CueR binding to the RP_O complex has a smaller dissociation constant of $K_{4\text{D}}$ (CueR-RP_O) ~ 15 nM, indicating the enhanced holo-CueR binding to P*copA* by RNAP. Similar enhancement by RNAP to apo-CueR binding to P*copA* is also observed.

Table S1. Thermodynamic equilibrium constants for interactions between P*copA*, RNAP, and (holo or apo) CueR as outlined in Fig. S15 from analyzing the population ratios determined from E_{FRET} histograms

Dissociation constants (nM)	RNAP-P*copA* interactions	
$K_{1\text{D}}$ (RP_{DE})	30 ± 3[a]	
$K_{2\text{D}}$ (RP_O)	105 ± 26[a]	
	CueR interactions with RNAP-P*copA* complex	
	Holo-CueR	Apo-CueR
$K_{3\text{D}}$ ($\text{CueR-RP}_{\text{DE}}$)	155 ± 32	111 ± 31
$K_{4\text{D}}$ (CueR-RP_O)	15 ± 5	141 ± 79
	RNAP interactions with CueR-P*copA* complex	
	Holo-CueR	Apo-CueR
$K_{5\text{D}}$ ($\text{CueR-RP}_{\text{DE}}$)	29 ± 16	28 ± 26
$K_{6\text{D}}$ (CueR-RP_O)	34 ± 20	16 ± 9

	CueR-P*copA* interactions	
	Holo-CueR	Apo-CueR
K_{7D} (CueR-P)	52 ± 10	152 ± 66

[a]Note that the values of K_{1D} and K_{2D} from population analysis here are within error bar of those in Table 1 in the main text, which are determined from the kinetic rate constants.

12. Additional references

1. Outten FW, Outten CE, Hale J, & O'Halloran TV (2000) Transcriptional Activation of An *Escherichia coli* Copper Efflux Regulation by the Chromosomal MerR Homologue, CueR. *J. Biol. Chem.* 275:31024.
2. O'Halloran TV, Frantz B, Shin MK, Ralston DM, & Wright JG (1989) The MerR Heavy Metal Receptor Mediates Positive Activation in a Topologically Novel Transcription Complex. *Cell* 56(1):119.
3. Hudson BP*, et al.* (2009) Three-Dimensional EM Structure of an Intact Activator-Dependent Transcription Initiation Complex. *Proc. Natl. Acad. Sci. U.S.A.* 106(47):19830-19835.
4. Changela A*, et al.* (2003) Molecular Basis of Metal-Ion Selectivity and Zeptomolar Sensitivity by CueR. *Science* 301:1383.
5. Newberry KJ & Brennan RG (2004) The Structural Mechanism for Transcription Activation by MerR Family Member Multidrug Transporter Activation, N-Terminus. *J. Biol. Chem.* 279:20356.
6. Kliegman JI, Griner SL, Helmann JD, Brennan RG, & Glasfeld A (2006) Structural Basis for the Metal-Selective Activation of the Manganese Transport Regulator of *Bacillus subtilis*. *Biochemistry* 45:3493.
7. Owens JT*, et al.* (1998) Mapping the σ^{70} Subunit Contact Sites on *Escherichia coli* RNA Polymerase with a σ^{70}-Conjugated Chemical Protease. *Proc. Natl. Acad. Sci. U.S.A.* 95(11):6021-6026.
8. Mekler V*, et al.* (2002) Structural Organization of Bacterial RNA Polymerase Holoenzyme and the RNA Polymerase-Promoter Open Complex. *Cell* 108(5):599-614.
9. Callaci S, Heyduk E, & Heyduk T (1998) Conformational Changes of *Escherichia coli* RNA Polymerase σ^{70} Factor Induced by Binding to the Core Enzyme. *J. Biol. Chem.* 273(49):32995-33001.
10. Bown JA*, et al.* (1999) Organization of Open Complexes at *Escherichia coli* Promoters: Location of Promoter DNA Sites Close to Region 2.5 of the σ^{70} Subunit of RNA Polymerase. *J. Biol. Chem.* 274(4):2263-2270.
11. Mukhopadhyay J*, et al.* (2003) Fluorescence Resonance Energy Transfer (FRET) in Analysis of Transcription-Complex Structure and Function. *Meth. Enzymol.* 371:144-159.
12. Kapanidis AN*, et al.* (2005) Retention of Transcription Initiation Factor σ^{70} in Transcription Elongation: Single-Molecule Analysis. *Mol. Cell* 20(3):347-356.
13. Robb NC*, et al.* (2013) The Transcription Bubble of the RNA Polymerase–Promoter Open Complex Exhibits Conformational Heterogeneity and Millisecond-Scale Dynamics: Implications for Transcription Start-Site Selection. *J. Mol. Biol.* 425(5):875-885.
14. Joshi CP*, et al.* (2012) Direct Substitution and Assisted Dissociation Pathways for Turning Off Transcription by a MerR-Family Metalloregulator. *Proc. Natl. Acad. Sci. U.S.A.* 109(38):15121-15126.
15. Brenner AJ & Harris ED (1995) A Quantitative Test for Copper Using Bicinchoninic Acid. *Anal. Biochem.* 226:80.
16. Outten CE, Outten FW, & O'Halloran TV (1999) DNA Distortion Mechanism for Transcriptional Activation by ZntR, A Zn(II)-responsive MerR Homologue in *Escherichia coli*. *J. Biol. Chem.* 274:37517.

17. Caslake LF, Ashraf SI, & Summers AO (1997) Mutations in the Alpha and Sigma-70 Subunits of RNA Polymerase Affect Expression of the *mer* Operon. *J. Bacteriol.* 179(5):1787-1795.
18. Andoy NM, *et al.* (2009) Single-Molecule Study of Metalloregulator CueR-DNA Interactions Using Engineered Holliday Junctions. *Biophys. J.* 97:97, 844.
19. Chung SH & Kennedy RA (1991) Forward-Backward Non-Linear Filtering Technique for Extracting Small Biological Signals from Noise. *Journal of Neuroscience Methods* 40(1):71-86.
20. Haran G (2004) Noise Reduction in Single-Molecule Fluorescence Trajectories of Folding Proteins. *Chem. Phys.* 307(2–3):137-145.
21. Nan X, Sims PA, Chen P, & Xie XS (2005) Observation of Individual Microtubule Motor Steps in Living Cells with Endocytosed Quantum Dots. *J. Phys. Chem. B* 109:24220.
22. Joo C & Ha T (2012) Preparing Sample Chambers for Single-Molecule FRET. *Cold Spring Harbor Protocols* 2012(10):pdb.prot071530.
23. Ralston DM & O'Halloran TV (1990) Ultrasensitivity and Heavy-Metal Selectivity of the Allosterically Modulated MerR Transcription Complex. *Proc. Natl. Acad. Sci. U.S.A.* 87:3846.
24. Aitken CE, Marshall RA, & Puglisi JD (2008) An Oxygen Scavenging System for Improvement of Dye Stability in Single-Molecule Fluorescence Experiments. *Biophys. J.* 94(5):1826-1835.
25. deHaseth PL, Zupancic ML, & Record MT (1998) RNA Polymerase-Promoter Interactions: the Comings and Goings of RNA Polymerase. *J. Bacteriol.* 180(12):3019-3025.
26. DeHaseth PL, Lohman TM, Burgess RR, & Record MT (1978) Nonspecific Interactions of *Escherichia coli* RNA Polymerase with Native and Denatured DNA: Differences in the Binding Behavior of Core and Holoenzyme. *Biochemistry* 17(9):1612-1622.
27. Klumpp S & Hwa T (2008) Growth-Rate-Dependent Partitioning of RNA Polymerases in Bacteria. *Proc. Natl. Acad. Sci. U.S.A.* 105(51):20245-20250.
28. Grigorova IL, Phleger NJ, Mutalik VK, & Gross CA (2006) Insights into Transcriptional Regulation and σ Competition from an Equilibrium Model of RNA Polymerase Binding to DNA. *Proc. Natl. Acad. Sci. U.S.A.* 103(14):5332.